ARTICLES
https://doi.org/10.1038/s41928-018-0058-4
nature electronics

Field-effect transistors made from solution-grown two-dimensional tellurene

Yixiu Wang[1,9], Gang Qiu[2,3,9], Ruoxing Wang[1,9], Shouyuan Huang[4], Qingxiao Wang[5], Yuanyue Liu[6,7,8], Yuchen Du[2,3], William A. Goddard III[6], Moon J. Kim[4], Xianfan Xu[3,4], Peide D. Ye[2,3]* and Wenzhuo Wu[1,3]*

The reliable production of two-dimensional (2D) crystals is essential for the development of new technologies based on 2D materials. However, current synthesis methods suffer from a variety of drawbacks, including limitations in crystal size and stability. Here, we report the fabrication of large-area, high-quality 2D tellurium (tellurene) using a substrate-free solution process. Our approach can create crystals with process-tunable thickness, from a monolayer to tens of nanometres, and with lateral sizes of up to 100 μm. The chiral-chain van der Waals structure of tellurene gives rise to strong in-plane anisotropic properties and large thickness-dependent shifts in Raman vibrational modes, which is not observed in other 2D layered materials. We also fabricate tellurene field-effect transistors, which exhibit air-stable performance at room temperature for over two months, on/off ratios on the order of 10^6, and field-effect mobilities of about 700 $cm^2 V^{-1} s^{-1}$. Furthermore, by scaling down the channel length and integrating with high-*k* dielectrics, transistors with a significant on-state current density of 1 A mm^{-1} are demonstrated.

The continuing exploration of the properties of two-dimensional (2D) materials[1–4] and the integration of these materials into new technologies[5–8] requires reliable synthesis methods. The potential of scaling up existing approaches, however, remains uncertain[9,10]. This is due to factors such as the growth substrates and conditions[11–13], small crystal sizes[14] and the instability of the synthesized materials[11,15,16]. For example, top-down liquid-phase exfoliation is a promising approach for the production of large quantities of various atomically thin layered materials[14], including graphene, transition metal dichalcogenides and boron nitride. However, poor control over thickness uniformity and the small size of the derived materials undermines the viability of the approach. Control of nucleation and growth during the bottom-up chemical vapour deposition (CVD) process can lead to high-quality crystals of graphene[9] and MoS_2 (ref. [10]) with controlled thicknesses over a centimetre-sized lateral area. However, the method requires high growth temperatures and delicate control of the growth atmosphere, which limits its potential for scale-up. The epitaxial growth of ultrathin materials with exotic electronic properties, such as silicene[11], borophene[12] and stanene[13], has also been explored, although the need for substrates suitable for epitaxial growth and the stringent requirements of an ultrahigh-vacuum system increase the complexity of the synthesis.

Group VI tellurium has a unique chiral-chain crystal lattice in which individual helical chains of Te atoms are stacked together by van der Waals type bonds and spiral around axes parallel to the [0001] direction at the centre and corners of the hexagonal elementary cell[17] (Fig. 1a). Each tellurium atom is covalently bonded with its two nearest neighbours on the same chain. Earlier studies revealed that bulk Te has small effective masses and high hole mobilities due to spin–orbit coupling[18]. The lone-pair and anti-bonding orbitals give rise to a slightly indirect bandgap in the infrared regime (~0.35 eV) in bulk Te[19], which has a conduction band minimum (CBM) located at the H point of the Brillouin zone, and a valence band maximum (VBM) that is slightly shifted from the H point along the chain direction, giving rise to hole pockets near the H point[20]. When the thickness is reduced, the indirect feature becomes more prominent, as shown by our first-principles calculations (see Methods for computation details). For example, the VBM of four-layer Te is further shifted to (0.43, 0.34) (in the unit of the surface reciprocal cell), while the CBM remains at (1/2, 1/3) (Fig. 1b, inset). Accompanied by the shift of the VBM, the bandgap also increases (see Methods and Supplementary Fig. 1) due to the quantum confinement effect, and eventually reaches ~1 eV for monolayer Te[21]. Te has other appealing properties, such as its photoconductivity[22], thermoelectricity[20] and piezoelectricity[23], for applications in sensors, optoelectronics and energy devices. A wealth of synthetic methods have been developed to derive Te nanostructures[24–26], which favour the 1D form due to the inherent structural anisotropy in Te. Much less is known about the 2D form of Te and its related properties.

In this Article, we report a substrate-free solution process for synthesizing large-area, high-quality 2D Te crystals (termed tellurene) with a thickness of a monolayer to tens of nanometres and a unique chiral-chain van der Waals structure that is fundamentally different from layered van der Waals materials.

Synthesis and structural characterization of 2D tellurene

We use the term X-ene to describe 2D forms of elemental materials without considering the specific bonding[21,27]. The samples are

[1]School of Industrial Engineering, Purdue University, West Lafayette, IN, USA. [2]School of Electrical and Computer Engineering, Purdue University, West Lafayette, IN, USA. [3]Birck Nanotechnology Center, Purdue University, West Lafayette, IN, USA. [4]School of Mechanical Engineering, Purdue University, West Lafayette, IN, USA. [5]Department of Materials Science and Engineering, University of Texas at Dallas, Richardson, TX, USA. [6]The Resnick Sustainability Institute, California Institute of Technology, Pasadena, CA, USA. [7]Materials and Process Simulation Center, California Institute of Technology, Pasadena, CA, USA. [8]Texas Materials Institute, Department of Mechanical Engineering, The University of Texas at Austin, Austin, TX, USA. [9]These authors contributed equally: Yixiu Wang, Gang Qiu and Ruoxing Wang *e-mail: yep@purdue.edu; wenzhuowu@purdue.edu

© 2018 Macmillan Publishers Limited, part of Springer Nature. All rights reserved.

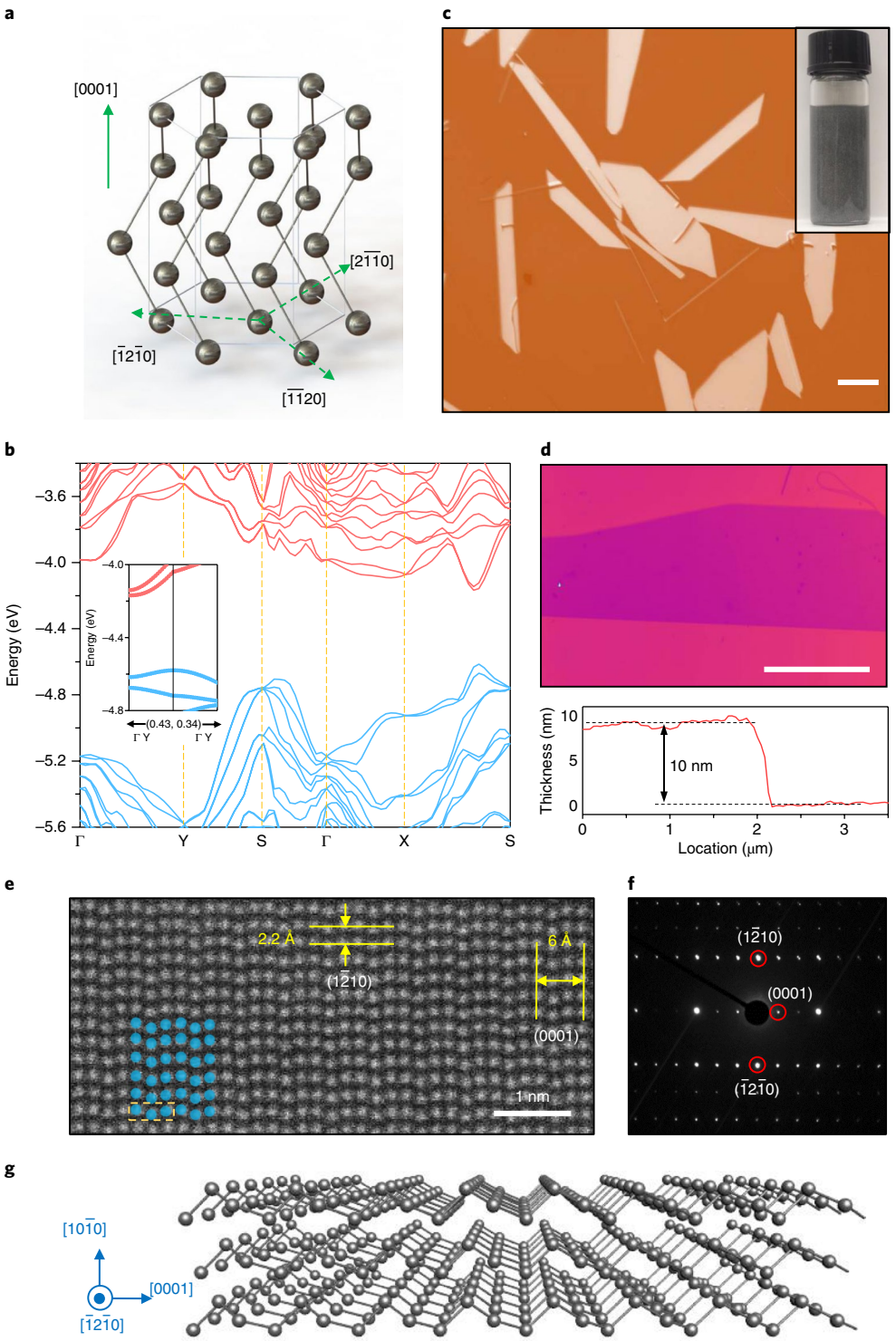

Fig. 1 | Solution-grown large-area 2D Te and material characterization. a, Atomic structure of Te. **b**, Band structure of four-layer Te, calculated using the Perdew–Burke–Ernzerhof (PBE) functional. Valence bands are shown in blue, and conduction bands are in red. Inset, Local band structure near the VBM; Γ, (0,0); X, (0.5, 0); Y, (0, 0.5); S, (0.5, 0.5); all in units of the surface reciprocal lattice vectors. See the Methods section entitled 'first-principles calculations' for further information about the electronic structure. **c**, Optical image of solution-grown Te flakes. Inset, Optical image of the Te solution dispersion. Scale bar, 20 μm. **d**, Atomic force microscope (AFM) image of a 10 nm 2D Te flake. Scale bar, 30 μm. **e**, HAADF–STEM image of tellurene. False-coloured (in blue) atoms are superimposed on the original STEM image to highlight the helical structure. **f**, Diffraction pattern of tellurene. **g**, 3D illustration of the structure of tellurene.

grown through the reduction of sodium tellurite (Na_2TeO_3) by hydrazine hydrate (N_2H_4) in an alkaline solution at temperatures from 160 to 200 °C, in the presence of crystal-face-blocking ligand polyvinylpyrrolidone (PVP) (see Methods). The inset to Fig. 1c presents an optical image of a typical tellurene solution dispersion after reactions at 180 °C for 20 h when the Na_2TeO_3:PVP mole ratio

© 2018 Macmillan Publishers Limited, part of Springer Nature. All rights reserved.

is 52.4:1 (see Methods). The 2D Te flakes can be transferred and assembled at large scale into a single-layer continuous thin film through a Langmuir–Blodgett (LB) process[28] or into a networked continuous thin film[8,29,30] through ink-jet printing (see Methods) onto various substrates (Supplementary Fig. 2) for future characterization and device integration. It should be noted that current LB approaches still lack certain desired capabilities in terms of film continuity and uniformity when compared to other methods such as ink-jet printing[8,29,30] for assembling solution-derived 2D materials into high-performance devices. These preliminary results (Supplementary Fig. 2) show potential and warrant more systematic work for future large-scale assembly and applications of solution-derived 2D functional materials.

Our individual 2D flakes have edge lengths ranging from 50 to 100 μm and thicknesses from 10 to 100 nm (Fig. 1d and Supplementary Fig. 3). The structure, composition and quality of these tellurene crystals were analysed by high-angle annular dark-field scanning transmission electron microscopy (HAADF–STEM), high-resolution transmission electron microscopy (HRTEM), energy-dispersive X-ray spectroscopy (EDS) and X-ray diffraction (XRD) (Fig. 1e,f and Supplementary Fig. 4). Figure 1e shows a typical atomically resolved HAADF–STEM image of a tellurene flake (see Methods). The helical chains and a threefold screw symmetry along ⟨0001⟩ are visible (Fig. 1e). The interplanar spacings are 2.2 Å and 6.0 Å, corresponding to Te $(1\bar{2}10)$ and (0001) planes[31], respectively. Figure 1f presents a selective area electron diffraction (SAED) pattern along the $[10\bar{1}0]$ zone axis, which is perpendicular to the top surface of the flake. No point defects or dislocations were observed over a large area within single crystals (Supplementary Fig. 4). EDS result confirmed the chemical composition of Te (Supplementary Fig. 4). Similar characterizations and analyses of dozens of 2D flakes with different sizes indicate that all samples grow laterally along the ⟨0001⟩ and $\langle 1\bar{2}10\rangle$ directions, with vertical stacking along the $\langle 10\bar{1}0\rangle$ direction (Fig. 1g).

Growth mechanism and geometric control of 2D tellurene

Control of PVP concentration is key to obtaining 2D tellurene. Figure 2a shows the productivity (see Methods) of tellurene grown at 180 °C versus time for a broad range of Na_2TeO_3/PVP mole ratios. When a smaller amount of PVP is used, the first 2D structures appear after a shorter reaction time (Fig. 2a and Supplementary Fig. 5). A closer examination of reactions with different PVP concentrations reveals an intriguing morphology evolution in growth products with time. For each PVP concentration, the initial growth products are dominantly 1D nanostructures (Fig. 2b and Supplementary Fig. 5), similar to previous reports[24–26]. After a certain period of reaction, structures possessing both 1D and 2D characteristics start to emerge (Fig. 2b and Supplementary Fig. 5). TEM characterizations indicate that the long axes (showing 1D characteristics) of these flakes are ⟨0001⟩ oriented, and the lateral protruding regions (showing 2D characteristics) grow along the $\langle 1\bar{2}10\rangle$ direction, with the $\{10\bar{1}0\}$ facets as the top/bottom surfaces (Supplementary Fig. 6). The 2D regions are enclosed by edges with atomic-level step roughness (Supplementary Fig. 6). These high energy edges are not specific to certain planes during the intermediate states. These structures also have more uneven surfaces than 2D tellurene (Supplementary Fig. 6), further manifesting their intermediate nature. Finally, the ratio of 2D tellurene flakes with a straight $\{1\bar{2}10\}$ edge increases with a reduction in 1D and intermediate structures (Supplementary Fig. 5), and reaches a plateau after an extended period of growth, for example, ~30 h (Fig. 2a and Supplementary Fig. 5). Growth with a lower level of PVP has a smaller final productivity (Fig. 2a and Supplementary Fig. 5). The observed morphology evolution suggests that the balance between kinetic and thermodynamic growth dictates the transformation from 1D structures to 2D forms (Fig. 2b). In the initial growth, PVP is preferentially adsorbed on the $\{10\bar{1}0\}$ surfaces of the nucleated seeds[26], which promotes kinetic-driven 1D growth (Supplementary Fig. 5). As the reaction continues, $\{10\bar{1}0\}$ surfaces of the formed structures would become partially covered due to insufficient PVP capping. Because the $\{10\bar{1}0\}$ surfaces have the lowest free energy in tellurium[32], the growth of $\{10\bar{1}0\}$ surfaces along the $\langle 1\bar{2}10\rangle$ direction significantly increases through thermodynamic-driven assembly, giving rise to the observed intermediate structures. Enhanced growth along the $\langle 1\bar{2}10\rangle$ direction together with continued ⟨0001⟩ growth (Supplementary Fig. 6) leads to the formation of 2D tellurene (Supplementary Fig. 5 and Fig. 2b).

The sizes and thicknesses of tellurene can also be effectively modulated by controlling the ratio between sodium tellurite and PVP (Fig. 2c and Supplementary Fig. 7). The width of tellurene monotonically decreases with a reduction in PVP level. This thickness is minimized when a medium level of PVP is used (for example, a Na_2TeO_3/PVP ratio of ~52.4:1, group 12 in Fig. 2c and Supplementary Fig. 7), and increases with both an increase and decrease of PVP from this medium level (Fig. 2c). With a small amount of PVP, the solution is supersaturated with Te source, and homogeneous nucleation of Te can occur on a large scale, consuming resources for subsequent growth. As a result, the Ostwald ripening of Te nuclei is shortened, and the final tellurene crystals have smaller sizes than samples grown at higher PVP concentrations. The low PVP level also leads to more significant growth along thickness directions. On the other hand, when the PVP level is high, the fewer nucleation events allow a sufficient supply of Te source for subsequent growth, leading to increased width and thickness. Also, the productivity of tellurene increases with the reaction temperature from 160 to 180 °C (Supplementary Fig. 8). This is probably because a higher temperature promotes the forward reaction rate in the half reaction of endothermic hydrazine oxidation (Supplementary Notes). However, when the temperature increases from 180 to 200 °C, possible breaking of the van der Waals bonds between Te chains by the excessive energy could lead to saturated productivity.

Tellurene crystals with a thickness smaller than 10 nm and ultimately a monolayer structure can be further derived through a solvent-assisted post-growth thinning process (see Methods). The thickness of the tellurene decreases with time after acetone is introduced into the growth solution (Supplementary Fig. 9). After 6 h, the average thickness of tellurene is reduced to ~10 nm, with the thinnest flake 4 nm thick (~10 layers) (Supplementary Fig. 9). Due to their poor solubility in acetone, PVP molecules tend to desorb from the tellurene and undergo aggregation[33], giving rise to the sedimentation of tellurene over time in acetone (Supplementary Fig. 9). Lacking the protection of PVP, the tellurene surfaces become exposed and react with the alkaline growth solution (pH of ~11.5)[34], leading to the reduced thickness. We also performed control experiments using other types of solvent in the growth solution (Supplementary Fig. 10), the results of which suggest that PVP solubility in the solvent significantly affects the above process. Large-area (up to 100 μm in lateral dimensions) tellurene crystals with monolayer, bilayer, trilayer and few-layer thickness can also be obtained (Fig. 2d and Supplementary Fig. 11) by controlling the pH values of the tellurene dispersion solution in the above post-growth thinning process (see Methods, Fig. 2d and Supplementary Fig. 12).

Thickness- and angle-dependent Raman spectra

These high-quality ultrathin tellurene crystals with controlled thickness provide an ideal system to explore their intrinsic properties in the 2D limit. We first characterized the optical properties of as-synthesized tellurene with a wide range of thickness (from monolayer to 37.4 nm) by angle-resolved polarized Raman spectroscopy at room temperature (see Methods). The incident light enters along the $[10\bar{1}0]$ direction and is polarized into the [0001] helical chain direction of the tellurene. The Raman spectra of tellurene samples with different thickness (Fig. 3a) exhibit three main

© 2018 Macmillan Publishers Limited, part of Springer Nature. All rights reserved.

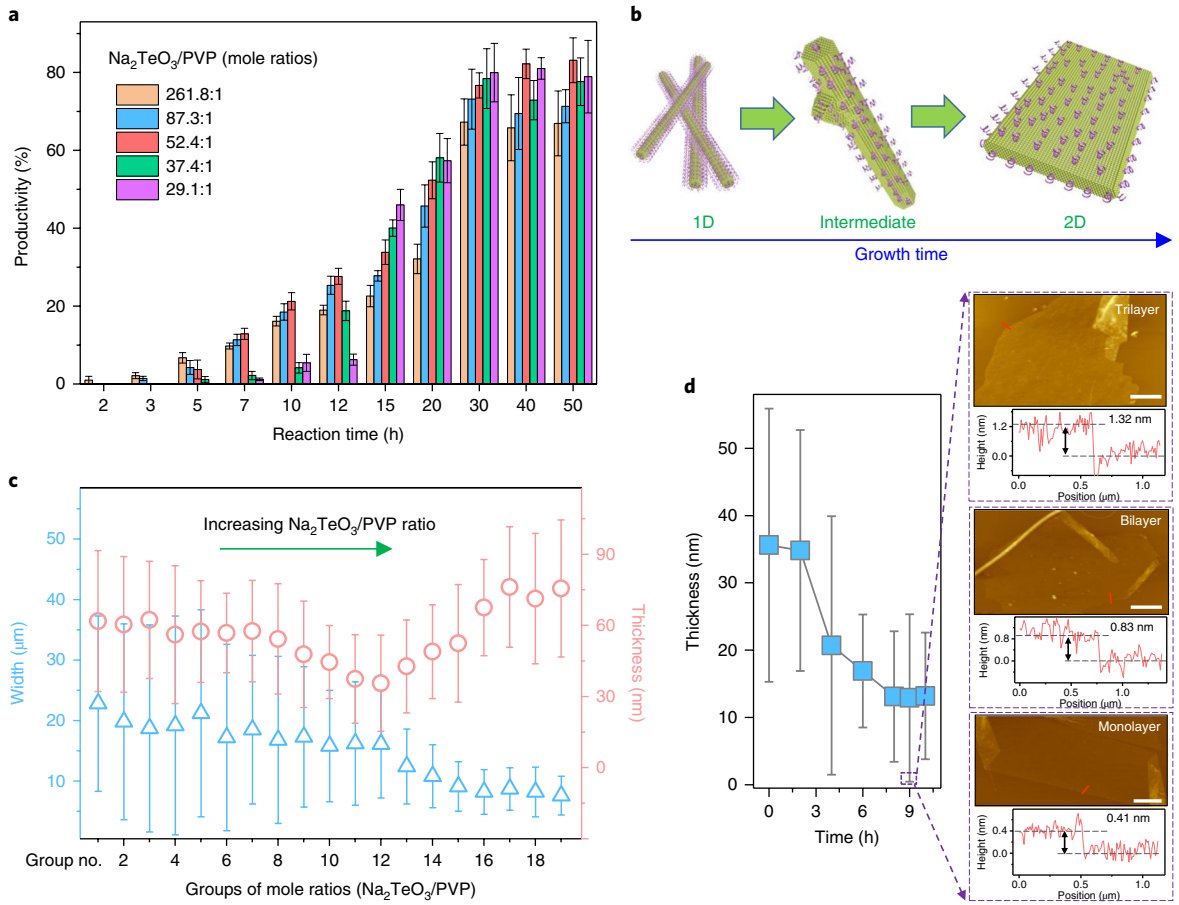

Fig. 2 | Solution processing for tellurene. a, Growth outcome for different PVP concentrations with different reaction times. Mean values from five technical replicates are shown. Error bars represent s.d. **b**, Morphology evolution from 1D Te structures to 2D Te. **c**, Thickness and width modulation of 2D Te. Mean values from eight technical replicates are shown. Error bars represent s.d. **d**, Post-growth thinning process with solution pH10.5 to obtain ultrathin few-layer and monolayer tellurene. Scale bars, 5 μm. Mean values from eight technical replicates are shown. Error bars represent s.d.

Raman-active modes—one A-mode and two E-modes—which correspond to chain expansion in the basal plane, bond-bending around the [1$\bar{2}$10] direction, and asymmetric stretching mainly along the [0001] helical chain[35], respectively (Supplementary Fig. 13). For 2D Te samples thicker than 20.5 nm, three Raman-active modes located at 92 cm^{-1} (E_1 transverse (TO) phonon mode), 121 cm^{-1} (A_1 mode) and 143 cm^{-1} (E_2 mode) were identified (Fig. 3a), which agree well with previous observations in bulk and nanostructured tellurium[36–38], indicating that although these thicker crystals possess 2D morphology, their symmetric properties can still be characterized as bulk. The appreciable effective dynamic charge induced for the E_1 mode in tellurium leads to a split of E_1 doublets at 92 cm^{-1} and 105 cm^{-1} for transverse (TO) or longitudinal (LO) phonons, respectively[37]. The absence of the E_1 (LO) mode in our observed results for 2D Te thicker than 20.5 nm, similar to previous reports on bulk and nanostructured tellurium[36–38], may be attributed to the different signs in the deformation potential and the electro-optic contribution to the Raman scattering tensor, giving rise to cancellation if both contributions have the same magnitude[39]. As the thickness decreases from 20.5 to 9.1 nm (Fig. 3a), the deformation potential in the tellurene lattice increases while the electro-optic effect weakens[40], leading to the appearance of the E_1 (LO) mode in the Raman spectra for 2D Te crystals with intermediate thickness. When the thickness of the 2D Te further reduces (smaller than 9.1 nm in Fig. 3a), degeneracy in the E_1 TO and LO modes occurs with peak broadening, possibly due to the intra-chain atomic displacement, the electronic band structure changes and the symmetry assignments for each band[41], all of which are affected by the sample thickness.

When the thickness of tellurene decreases, there are significant blueshifts for both A_1 (shift to 136 cm^{-1} for monolayer) and E_2 (shift to 149 cm^{-1} for monolayer) modes (Fig. 3a). The hardened in-plane E_2 vibration mode in thinner tellurene, similar to reported observations for black phosphorus[42] and MoS_2 (ref. [43]), may be attributed to the enhanced interlayer long-range Coulombic interactions when thinned down. The observed blueshift for the A_1 mode in 2D Te, in strong contrast to 2D layered van der Waals materials, which usually show a redshift for the out-of-plane vibration mode when thinned down[15,42,43], is thought to be closely related to the unique chiral-chain van der Waals structure of tellurene. When thinned down, the lattice deformation within the 2D plane gives rise to the attenuated inter-chain van der Waals interactions and enhanced intra-chain covalent interactions in the individual tellurene layer, leading to more effective restoring forces on tellurium atoms and hence a hardened out-of-plane A_1 vibration mode (Supplementary Fig. 13). This unique structure of tellurene also results in the giant thickness-dependent shift in Raman vibrational modes, which is unseen in 2D layered van der Waals materials[42–44]. The interaction between the substrate (SiO_2/Si) and 2D Te flakes could also contribute to the hardened A_1 and E_2 modes[36]. Stiffening of vibrational modes in monolayer tellurene (Fig. 3a) is consistent with its structure reconstruction, where extra bonds are formed between neighbouring chains in the single-layer tellurium[21,27,45].

© 2018 Macmillan Publishers Limited, part of Springer Nature. All rights reserved.

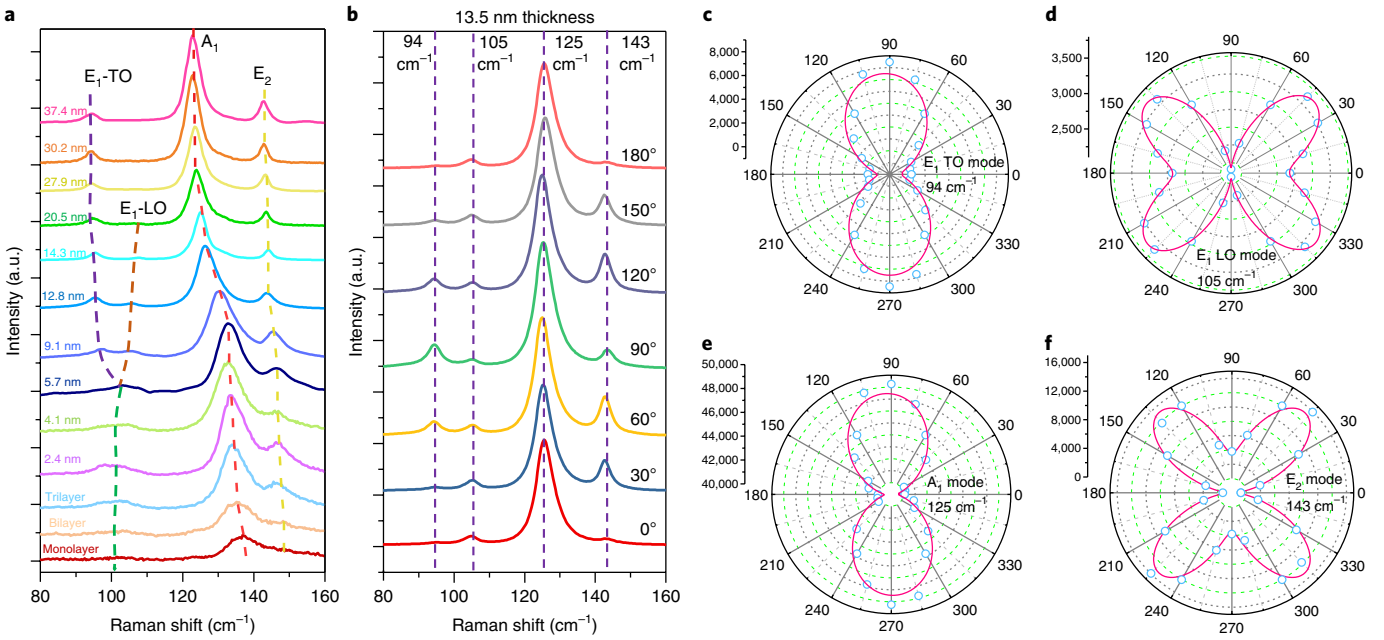

Fig. 3 | Angle-resolved Raman spectra for 2D tellurene with different thicknesses. a, Raman spectra for 2D Te with different thicknesses. **b**–**f**, Angle-resolved Raman spectra for a 13.5-nm-thick flake: evolution with angles between crystal orientation and incident laser polarization (**b**) and polar figures of Raman intensity corresponding to A_1 and two E modes located at 94 (E_1 TO), 105 (E_1 LO), 125 (A_1) and 143 (E_2) cm^{-1} (**c**–**f**). Fitting curves are described in the Supplementary Methods.

Reduced in-plane symmetry in the chiral-chain van der Waals structure of tellurene indicates a strong in-plane anisotropy for its material properties. We further characterized the anisotropic optical properties of as-synthesized tellurene with three different thicknesses (28.5, 13.5 and 9.7 nm) by angle-resolved polarized Raman spectroscopy at room temperature (see Methods). By rotating the tellurene flakes in steps of 15°, we observed changes in the angle-resolved Raman peak intensities (Fig. 3b and Supplementary Figs 14a and 15a). We extracted the peak intensities of different modes by fitting with a Lorentz function and plotted them into the corresponding polar figures (Fig. 3c–f, Supplementary Figs. 14b–e and 15b–d) (see Methods). Although all the modes change in intensity with polarization angle, we find that the peak for the A_1 mode in all samples exhibits the largest sensitivity to the relative orientation between the [0001] direction and the polarization of the excitation laser (middle panels of Fig. 3b and Supplementary Figs. 14a and 15a). It is worth noting that the direction of maximum intensity in the A_1 polar plot changes with sample thickness. More specifically, A_1 polar plots for the 13.5 and 28.5 nm samples show the maximum intensity at 90 and 270° along the [$1\bar{2}10$] direction (Fig. 3e and Supplementary Fig. 15c). However, when the thickness decreases to 9.7 nm, the maximum intensity direction switches to 0° and 180° along the [0001] direction (Supplementary Fig. 14d). A similar phenomenon also occurs for E_1 LO modes in the 13.5 and 9.7 nm samples (Fig. 3d and Supplementary Fig. 14c). Such thickness-dependent anisotropic Raman scattering could be attributed to the different absorption spectral range in the [0001] and [$1\bar{2}10$] directions[46] and the anisotropic interference effect[41]. The angle-resolved Raman results also confirm that the helical Te atom chains in the as-synthesized tellurene are oriented along the growth direction of the tellurene flake, matching the TEM results (Fig. 1e).

2D tellurene field-effect transistors

Finally, we explored the electrical performance of tellurene field-effect transistors (FETs) to demonstrate their great potential for logic electronics application. Back-gate devices were fabricated on high-k dielectric substrates, and source–drain regions were patterned by electron-beam lithography with the channel parallel to the [0001] direction of the tellurene (for details see Methods). We chose Pd/Au (50/50 nm) for the metal contacts because Pd has a relatively high workfunction that can reduce the contact resistance in p-type transistors[47–49]. Long-channel devices were first examined (channel length, 3 μm), where the contact resistance is negligible and the transistor behaviour is dominated by the intrinsic electrical properties of the channel material. Figure 4a presents the transfer curve of a typical 7.5-nm-thick 2D Te FET measured at room temperature. The device exhibits p-type characteristics with slight ambipolar transport behaviour due to its narrow-bandgap nature, with large drain current over 300 mA mm^{-1} (Supplementary Fig. 23) and high on/off ratio on the order of ~1×10^5. The p-type behaviour originates from the high level of the Te valence band edge, as shown by our first-principles calculations (Supplementary Fig. 16). Meanwhile, the process-tunable thickness of tellurene allows modulation of the electrical performance in tellurene transistors. Overall, the important metrics of tellurene-based transistors, such as on/off ratio, mobility and on-state current level, are superior or comparable to those of transistors based on other 2D materials[11,15,16,50]. We further investigated the thickness dependence of two key metrics of device performance—on/off ratio and field-effect mobility—for more than fifty 2D Te long-channel devices, with flake thickness ranging from over 35 nm to a monolayer (~0.5 nm), to elucidate the transport mechanism of 2D Te FETs (Fig. 4b). The linear behaviour of the output curves in the low V_{ds} region (Supplementary Fig. 23) suggests that the contact resistance is low (see Supplementary Notes and Supplementary Fig. 19 for the extracted contact resistance), which ensures the soundness of the extraction of field-effect mobility from the slope of the linear region of the transfer curves (see Methods). The field-effect mobilities of 2D Te transistors peak at ~700 cm^2 V^{-1} s^{-1} at room temperature at a thickness of about 16 nm and decrease gradually with a further increase in thickness. The transfer curves of thin devices with thickness of 2.8 nm (approximately six layers), 1.7 nm (approximately four layers), 1.0 nm (bilayer) and 0.5 nm (monolayer) are presented in Supplementary Fig. 24. A benchmark comparison with black

© 2018 Macmillan Publishers Limited, part of Springer Nature. All rights reserved.

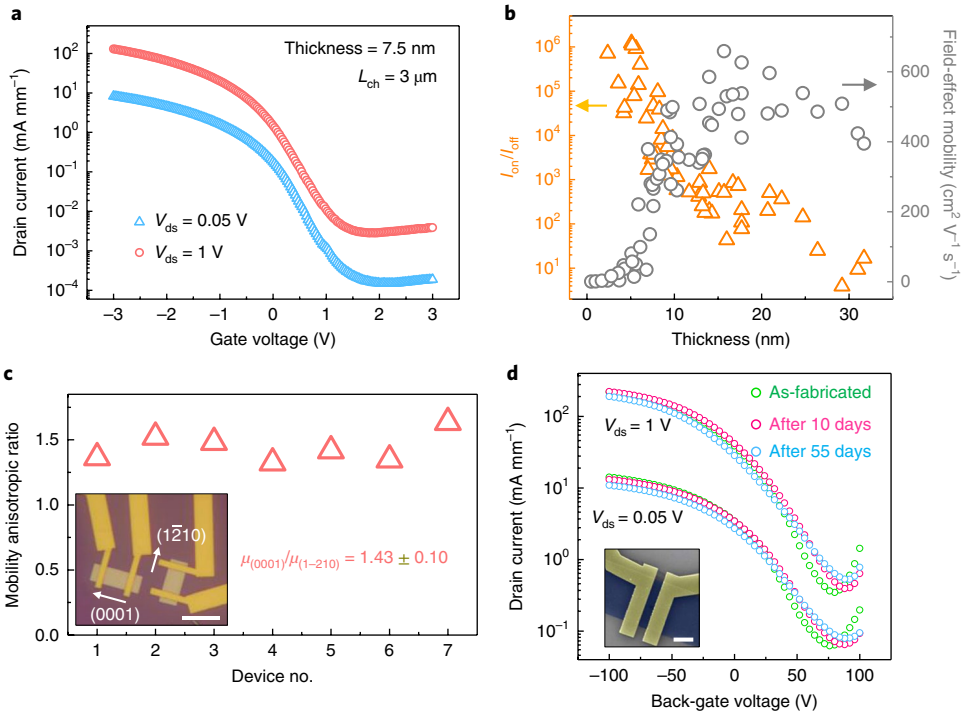

Fig. 4 | 2D tellurene FET device performance. a, Transfer curve of a typical long-channel 2D tellurene transistor with a thickness of 7.5 nm. **b**, Thickness-dependent on/off ratio (orange triangles) and field-effect mobility (grey circles) for 2D tellurene transistors. The non-monotonic dependence of mobility on thickness can be fitted using the Thomas–Fermi screening model (Supplementary Notes and Supplementary Fig. 20). **c**, Anisotropic mobility measurements along [0001] and [1$\bar{2}$10] directions. Inset, Optical image of a typical device for anisotropic transport measurement. Scale bar, 10 μm. **d**, Transfer curves of a typical 2D tellurene transistor with a thickness of 15 nm, with stability measured for up to 55 days. Inset, False-coloured SEM image of a tellurene transistor. The scale bar is 10 μm.)

phosphorus, which is also a narrow-bandgap p-type 2D material, shows that solution-synthesized 2D Te has approximately two to three times higher mobility than black phosphorus when the same device structure, geometry and mobility extraction method are adopted[15] (Supplementary Fig. 21). This thickness dependence is similar to that of other layered materials that experience screening and interlayer coupling[15,16] (Supplementary Notes and Supplementary Fig. 20). The field-effect mobility is also affected by the contribution of the carriers from layers near the semiconductor–oxide interface. Thinner samples are more susceptible to charge impurities at the interface and surface scattering, which explains the decrease in the mobility of the few-layer tellurene transistors. We expect to be able to improve the mobility of tellurene through approaches such as improving the interface quality with high-k dielectrics[51] or hexagonal boron nitride encapsulation to reduce the substrate phonon scattering and charge impurity. For bilayered tellurene transistors, the external field-effect mobility is reduced to ~1 cm^2 V^{-1} s^{-1}. This is due to the bandgap increasing in few-layer tellurene to form a much higher Schottky barrier, which may introduce a large deviation in extracting mobility due to the drastically increased contact resistance. Because of the reduced gate electrostatic control in thicker flakes, the thickness-dependent on/off ratios (Supplementary Notes) steeply decrease from ~1×10^6 to less than 10 once the crystal thickness approaches the maximum depletion width of the films, with a trend similar to other reported narrow-bandgap depletion-mode 2D FETs[15,16].

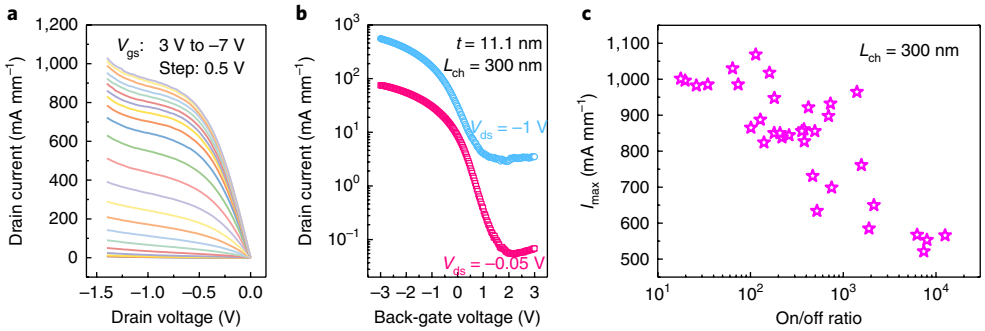

Fig. 5 | High on-state current density in short-channel tellurene devices. a,**b**, Output (**a**) and transfer (**b**) curves of an 11.1-nm-thick tellurene transistor with 300 nm channel. **c**, Trade-off between on/off ratio and maximum drain current measured in over 30 short-channel devices with the same geometry and dimension as in **a** and **b**. The maximum drain current of several devices surpassed 1 A mm^{-1}.

© 2018 Macmillan Publishers Limited, part of Springer Nature. All rights reserved.

The in-plane anisotropic electrical transport properties were also studied at room temperature. To minimize flake-to-flake variation and geometric non-ideality, we applied a dry-etching method (see Methods) to trim two identical rectangles from the same 2D Te flake. One of the rectangles was aligned along the 1D atomic chain [0001] direction and the other along the [$1\bar{2}10$] direction (Fig. 4c, inset). Long-channel FETs (channel length, 8 μm) were fabricated to minimize contact influence and manifest the intrinsic material properties. The extracted field-effect mobilities along these two primary directions from seven 2D Te samples exhibit an average anisotropic mobility ratio of 1.43 ± 0.10 (Fig. 4c). A typical set of results measured from a 22-nm-thick sample is shown in Supplementary Fig. 22. This anisotropic ratio in mobility is slightly lower than that reported for bulk tellurium[52], possibly due to the enhanced surface scattering in our ultrathin Te samples. Our first-principles calculations show a similar degree of anisotropy in the effective masses along these two orthogonal directions (Fig. 1b, $0.32m_0$ perpendicular to the chain and $0.30m_0$ along the chain; see Methods).

Great air stability was also demonstrated in tellurene transistors with different flake thicknesses. The electrical performance of a 15-nm-thick transistor was monitored after being exposed in air for two months without any encapsulation, as shown in Fig. 4d. No significant degradation was observed in the device during the two-month period, except a slight threshold voltage shift probably arising from sequential measurement variation. We also demonstrated that this good air stability is valid for almost the entire thickness range from thick flakes down to 3 nm (Supplementary Fig. 25). For flakes thinner than this, the films no longer conduct after the first couple of days.

More strikingly, by scaling down the channel length and integrating with our atomic-layer-deposition-grown high-k dielectric, we achieved a record-high drive current of over 1 A mm^{-1} at a relatively low $V_{ds} = 1.4$ V. Figure 5a,b presents I–V curves for a short-channel device with channel length of 300 nm fabricated on an 11-nm-thick Te flake. The on/off ratio at small drain bias ($V_{ds} = -0.05$ V) is over 1×10^3, which is still a decent value considering its narrow bandgap of ~0.4 eV (Supplementary Fig. 1). The off-state performance deteriorates slightly at large drain voltage ($V_{ds} = -1$ V, blue circles in Fig. 5b) due to the short-channel effect. A large drain voltage reduces the barrier height for n-type electron transport and the electron current is unhindered, which is also reflected in the upswing of drain current at large V_{ds} in the output curve (Fig. 5a). Such an effect is common in narrow-bandgap short-channel devices[53,54] and can be mediated through proper contact engineering[54]. Figure 5c shows the relationship between two key transistor parameters—on/off ratio and maximum drain current—for over 30 devices with different channel thicknesses. Generally speaking, a short-channel device with a flake thickness of around 7–8 nm offers the best performance, with an on/off ratio of $\sim 1 \times 10^4$ and maximum drain current of >600 mA mm^{-1}. It is also worth mentioning that the maximum drain current we achieved was 1.06 A mm^{-1}, with several devices exceeding 1 A mm^{-1}, which is the highest value achieved in any two-dimensional material transistor reported, to the best of our knowledge[53,55,56]. This number is also comparable to that of conventional semiconductor devices.

Conclusions

We have developed a simple, low-cost, solution-based approach for the scalable synthesis and assembly of 2D Te crystals. These high-quality 2D Te crystals have high carrier mobility and are air-stable (measured up to two months). Our prototypical 2D Te device shows a good all-around figure of merit (Supplementary Fig. 26 and Supplementary Table 1) compared to existing 2D materials, and record-high on-state current capacity. Our approach has the potential to produce stable, high-quality, ultrathin semiconductors with good control of composition, structure and dimensions, opening up opportunities for applications in electronics, optoelectronics, energy conversion and energy storage. 2D tellurene, as a chiral-chain van der Waals solid, adds a new class of nanomaterials to the large family of 2D crystals.

Methods

Synthesis of 2D tellurene crystals. In a typical procedure, analytical-grade Na_2TeO_3 (0.00045 mol) and an amount of PVP were placed into double-distilled water (33 ml) at room temperature under magnetic stirring to form a homogeneous solution. The resulting solution was poured into a Teflon-lined stainless-steel autoclave, which was then filled with an aqueous ammonia solution (25%, wt/wt%) and hydrazine hydrate (80%, wt/wt%). The autoclave was sealed and maintained at the reaction temperature for a designed time. The autoclave was then cooled to room temperature naturally. The resulting solid silver-grey products were precipitated by centrifugation at 5,000 r.p.m. for 5 min and washed three times with distilled water (to remove any ions remaining in the final product).

LB transfer of tellurene. The hydrophilic 2D Te nanoflake monolayers can be transferred to various substrates by the LB technique. The washed nanoflakes were suspended in a mixture solvent comprising *N*,*N*-dimethylformamide (DMF) and $CHCl_3$ (for example, in the ratio 1.3:1). The mixture solvent was then dropped into the deionized water. Too much DMF will result in the 2D Te sinking in the water. It is difficult to mix the DMF, $CHCl_3$ and 2D Te when there is too much $CHCl_3$. After evaporation of the solvent, a monolayer assembly of 2D Te flakes was observed at the air/water interface; this monolayer assembly of 2D Te could then be transferred onto a substrate.

First-principles calculations. Density functional theory calculations were performed using the Vienna Ab-initio Simulation Package (VASP)[57] with projector augmented-wave (PAW) pseudopotentials[58]. We used 500 eV for the plane-wave cutoff, 5x5x1 Monkhorst–Pack sampling, and fully relaxed the systems until the final force on each atom was less than 0.01 eV Å^{-1}. The Perdew–Burke–Ernzerhof exchange-correlation functional was used for relaxation of the system, and the Heyd–Scuseria–Ernzerhof functional was used to calculate the bandgaps (Supplementary Fig. 1) and band-edge levels (Supplementary Fig. 10). We found a significant structural reconstruction for monolayer Te, in agreement with reported results[21], but for bilayer and thicker Te the structure was similar to that of bulk Te. Our calculations show lattice parameters of 4.5 Å and 6.0 Å for multilayers, in agreement with experiments. The adsorption of O on bilayer Te and P was modelled using a 4 x 3 cell (Supplementary Fig. 12).

Structural characterization. The morphology of the ultrathin tellurene crystals was identified by optical microscopy (Olympus BX-60). The thickness was determined by atomic force microscopy (Keysight 5500). High-resolution STEM/TEM imaging and SAED were performed using a probe-corrected JEM-ARM 200F (JEOL USA) operated at 200 kV, and EDS data were collected by an X-MaxN100TLE detector (Oxford Instruments). In HAADF–STEM mode, the convergence semi-angle of the electron probe was 24 mrad, and the collection angle for the ADF detector was set to 90–370 mrad.

Determination of tellurene productivity. To quantify the 2D tellurene flake ratio, we measured all products using the same process. Freshly prepared 2D tellurene solution (1 ml) was centrifuged at 5,000 r.p.m. for 5 min after adding acetone (2 ml), and washed twice with alcohol and double-distilled water. The 2D tellurene flakes were dispersed into 3 ml double-distilled water, then 100 μl dispersed solution was dropped onto a 1 × 1 cm^2 SiO_2/Si substrate. After water evaporation, an optical microscope recorded several images, randomly covering the 5 × 5 mm^2 area. Finally, we analysed the areas covered by 2D tellurene using ImageJ, a public-domain, Java-based image-processing program developed at the National Institutes of Health. We defined the productivity as the ratio of the 2D tellurene area with respect to the entire image area.

Solvent-assisted post-growth thinning process. For the thinning process using alkaline growth solution, as-synthesized 2D tellurene solution (1 ml) was mixed with acetone (3 ml) at room temperature. After a specific time (for example, 6 h), thin 2D tellurene was obtained by centrifugation at 5,000 r.p.m. for 5 min. Following application of the LB process, the 2D tellurene could be transferred onto a substrate.

For the thinning process using tellurene solution with controlled pH values, the suspension of as-synthesized 2D tellurene (1 ml) was centrifuged once with the addition of 3 ml deionized water. The 2D Te was dispersed into a solution of 1 ml NaOH and 3 ml acetone. The concentration of NaOH was varied to control the pH value of this 4 ml of solution. The solution was kept at room temperature for 2–10 h. Finally, the thinned tellurene samples were precipitated by centrifugation.

FET device fabrication and characterization. A high-k dielectric stack consisting of 20 nm hafnium zirconium oxide ($Hf_{0.5}Zr_{0.5}O_2$) and 2 nm Al_2O_3 was first deposited by atomic layer deposition onto heavily doped n^{++} silicon wafer. After

© 2018 Macmillan Publishers Limited, part of Springer Nature. All rights reserved.

transferring the tellurene flakes onto the substrate, source and drain regions were patterned by electron-beam lithography (EBL). We chose 50/50 nm Pd/Au for the contact metal because Pd has a relatively high workfunction that benefits p-type transistors by reducing the Schottky contact resistance. Electrical measurements were performed using a Keithley 4200A semiconductor characterization system.

By inserting numbers into the formula $\mu_{FE} = g_m L/WC_{ox}V_{ds}$, where g_m, L, W and C_{ox} are the transconductance, channel length, channel width and gate oxide capacitance, we can derive the field-effect mobilities for the tellurene transistors. Field-effect mobilities extracted from devices fabricated on tellurene crystals with various thicknesses are displayed in Fig. 4b. Devices for anisotropic transport measurement were first patterned with EBL into two perpendicular rectangles along the two principal in-plane directions of tellurene, and dry-etched into desired shapes with BCl_3 and argon plasma. The remainder of the fabrication process followed the same route as in high-k integrated FET devices[53].

Raman spectra. Angle-resolved Raman spectra were measured at room temperature. The crystal symmetry of Te renders one A_1 mode, one A_2 mode (Raman-inactive) and two doublet E modes at the Γ point of the Brillouin zone. The Raman signal was excited by a 633 nm He–Ne laser. Incident light entered along the [10$\bar{1}$0] direction, which is perpendicular to the Te flake surface and polarized into the [0001] direction, which is parallel to spiral atom chains (we denote this configuration as 0°). A linear polarizer was placed in front of the spectrometer to polarize reflected light into the same direction with incident light. The polarized Raman signal can eliminate all other superimposed Raman signals and manifests a clear trace of angle-dependent Raman spectrum evolution. By rotating the Te flake, we observed an angle-resolved Raman peak intensity change (Fig. 3a). We extracted the peak intensities of different modes by fitting with a Lorentz function and plotted them into polar figures (Fig. 3b–f). These angle-dependent behaviours were then fitted by carrying out matrix multiplication, $\mathbf{e}_i \times \mathbf{R} \times \mathbf{e}_r$, where $\mathbf{e}_i$ and $\mathbf{e}_r$ are unit vectors of the incident and reflected light direction and $\mathbf{R}$ is the Raman tensor of the corresponding Raman modes[2]. The angle-resolved Raman results confirm that the helical Te atom chain is indeed along the long axis of the Te flake, which matches our previous TEM results.

Data availability. The data that support the plots within this paper and other findings of this study are available from the corresponding author upon reasonable request.

Received: 25 October 2017; Accepted: 16 March 2018;
Published online: 17 April 2018

References

1. Castro Neto, A. H., Guinea, F., Peres, N. M. R., Novoselov, K. S. & Geim, A. K. The electronic properties of graphene. *Rev. Mod. Phys.* **81**, 109–162 (2009).
2. Qian, X., Liu, J., Fu, L. & Li, J. Quantum spin Hall effect in two-dimensional transition metal dichalcogenides. *Science* **346**, 1344–1347 (2014).
3. Chhowalla, M. et al. The chemistry of two-dimensional layered transition metal dichalcogenide nanosheets. *Nat. Chem.* **5**, 263–275 (2013).
4. Fiori, G. et al. Electronics based on two-dimensional materials. *Nat. Nanotech.* **9**, 768–779 (2014).
5. Wang, Q. H., Kalantar-Zadeh, K., Kis, A., Coleman, J. N. & Strano, M. S. Electronics and optoelectronics of two-dimensional transition metal dichalcogenides. *Nat. Nanotech.* **7**, 699–712 (2012).
6. Wu, W. et al. Piezoelectricity of single-atomic-layer MoS_2 for energy conversion and piezotronics. *Nature* **514**, 470–474 (2014).
7. Smith, R. J. et al. Large-scale exfoliation of inorganic layered compounds in aqueous surfactant solutions. *Adv. Mater.* **23**, 3944–3948 (2011).
8. Bonaccorso, F., Bartolotta, A., Coleman, J. N. & Backes, C. 2D-crystal-based functional inks. *Adv. Mater.* **28**, 6136–6166 (2016).
9. Hao, Y. et al. The role of surface oxygen in the growth of large single-crystal graphene on copper. *Science* **342**, 720 (2013).
10. Najmaei, S. et al. Vapour phase growth and grain boundary structure of molybdenum disulphide atomic layers. *Nat. Mater.* **12**, 754–759 (2013).
11. Tao, L. et al. Silicene field-effect transistors operating at room temperature. *Nat. Nanotech.* **10**, 227–231 (2015).
12. Mannix, A. J. et al. Synthesis of borophenes: anisotropic, two-dimensional boron polymorphs. *Science* **350**, 1513–1516 (2015).
13. Zhu, F.-F. et al. Epitaxial growth of two-dimensional stanene. *Nat. Mater.* **14**, 1020–1025 (2015).
14. Coleman, J. N. et al. Two-dimensional nanosheets produced by liquid exfoliation of layered materials. *Science* **331**, 568–571 (2011).
15. Liu, H. et al. Phosphorene: an unexplored 2D semiconductor with a high hole mobility. *ACS Nano* **8**, 4033–4041 (2014).
16. Li, L. et al. Black phosphorus field-effect transistors. *Nat. Nanotech.* **9**, 372–377 (2014).
17. von Hippel, A. Structure and conductivity in the VIb group of the periodic system. *J. Chem. Phys.* **16**, 372–380 (1948).
18. Doi, T., Nakao, K. & Kamimura, H. The valence band structure of tellurium. I. The k·p perturbation method. *J. Phys. Soc. Jpn* **28**, 36–43 (1970).
19. Coker, A., Lee, T. & Das, T. P. Investigation of the electronic properties of tellurium energy-band structure. *Phys. Rev. B* **22**, 2968–2975 (1980).
20. Peng, H., Kioussis, N. & Snyder, G. J. Elemental tellurium as a chiral p-type thermoelectric material. *Phys. Rev. B* **89**, 195206 (2014).
21. Zhu, Z. et al. Tellurene—a monolayer of tellurium from first-principles prediction. Preprint at https://arxiv.org/abs/1605.03253 (2016).
22. Liu, J.-W., Zhu, J.-H., Zhang, C.-L., Liang, H.-W. & Yu, S.-H. Mesostructured assemblies of ultrathin superlong tellurium nanowires and their photoconductivity. *J. Am. Chem. Soc.* **132**, 8945–8952 (2010).
23. Lee, T. I. et al. High-power density piezoelectric energy harvesting using radially strained ultrathin trigonal tellurium nanowire assembly. *Adv. Mater.* **25**, 2920–2925 (2013).
24. Mo, M. et al. Controlled hydrothermal synthesis of thin single-crystal tellurium nanobelts and nanotubes. *Adv. Mater.* **14**, 1658–1662 (2002).
25. Mayers, B. & Xia, Y. One-dimensional nanostructures of trigonal tellurium with various morphologies can be synthesized using a solution-phase approach. *J. Mater. Chem.* **12**, 1875–1881 (2002).
26. Qian, H.-S., Yu, S.-H., Gong, J.-Y., Luo, L.-B. & Fei, L.-f High-quality luminescent tellurium nanowires of several nanometers in diameter and high aspect ratio synthesized by a poly(vinyl pyrrolidone)-assisted hydrothermal process. *Langmuir* **22**, 3830–3835 (2006).
27. Xian, L., Paz, A. P., Bianco, E., Ajayan, P. M. & Rubio, A. Square selenene and tellurene: novel group VI elemental 2D semi-Dirac materials and topological insulators. *2D Mater.* **4**, 041003 (2017).
28. Zasadzinski, J. A., Viswanathan, R., Madsen, L., Garnaes, J. & Schwartz, D. K. Langmuir–Blodgett films. *Science* **263**, 1726–1733 (1994).
29. Hu, G. et al. Black phosphorus ink formulation for inkjet printing of optoelectronics and photonics. *Nat. Commun.* **8**, 278 (2017).
30. Kelly, A. G. et al. All-printed thin-film transistors from networks of liquid-exfoliated nanosheets. *Science* **356**, 69–73 (2017).
31. Cherin, P. & Unger, P. Two-dimensional refinement of the crystal structure of tellurium. *Acta Crystallogr.* **23**, 670–671 (1967).
32. Tran, R. et al. Surface energies of elemental crystals. *Sci. Data* **3**, 160080 (2016).
33. Lan, W.-J., Yu, S.-H., Qian, H.-S. & Wan, Y. Dispersibility, stabilization, and chemical stability of ultrathin tellurium nanowires in acetone: morphology change, crystallization, and transformation into TeO_2 in different solvents. *Langmuir* **23**, 3409–3417 (2007).
34. Liu, J.-W., Wang, J.-L., Wang, Z.-H., Huang, W.-R. & Yu, S.-H. Manipulating nanowire assembly for flexible transparent electrodes. *Angew. Chem. Int. Ed.* **53**, 13477–13482 (2014).
35. Martin, R. M., Lucovsky, G. & Helliwell, K. Intermolecular bonding and lattice dynamics of Se and Te. *Phys. Rev. B* **13**, 1383–1395 (1976).
36. Du, Y. et al. One-dimensional van der Waals material tellurium: Raman spectroscopy under strain and magneto-transport. *Nano Lett.* **17**, 3965–3973 (2017).
37. Pine, A. & Dresselhaus, G. Raman spectra and lattice dynamics of tellurium. *Phys. Rev. B* **4**, 356–371 (1971).
38. Wang, Q. et al. Van der Waals epitaxy and photoresponse of hexagonal tellurium nanoplates on flexible mica sheets. *ACS Nano* **8**, 7497–7505 (2014).
39. Richter, W. Extraordinary phonon Raman scattering and resonance enhancement in tellurium. *J. Phys. Chem. Solids* **33**, 2123–2128 (1972).
40. Qiu, J. & Jiang, Q. Film thickness dependence of electro-optic effects in epitaxial $Ba_{0.7}Sr_{0.3}TiO_3$ thin films. *J. Appl. Phys.* **102**, 074101 (2007).
41. Ling, X. et al. Anisotropic electron–photon and electron–phonon interactions in black phosphorus. *Nano Lett.* **16**, 2260–2267 (2016).
42. Wang, X. et al. Highly anisotropic and robust excitons in monolayer black phosphorus. *Nat. Nanotech.* **10**, 517–521 (2015).
43. Lee, C. Anomalous lattice vibrations of single- and few-layer MoS_2. *ACS Nano* **4**, 2695–2700 (2010).
44. Ferrari, A. C. et al. Raman spectrum of graphene and graphene layers. *Phys. Rev. Lett.* **97**, 187401 (2006).
45. Huang, X. et al. Epitaxial growth and band structure of Te film on graphene. *Nano Lett.* **17**, 4619–4623 (2017).
46. Isomäki, H. & von Boehm, J. Optical absorption of tellurium. *Phys. Scripta* **25**, 801–803 (1982).
47. Deng, Y. et al. Towards high-performance two-dimensional black phosphorus optoelectronic devices: the role of metal contacts. *2014 IEEE Int. Electron Devices Meet.* https://doi.org/10.1109/IEDM.2014.7046987 (IEEE, 2015).
48. Liu, Y., Xiao, H. & Goddard, W. A. Schottky-barrier-free contacts with two-dimensional semiconductors by surface-engineered MXenes. *J. Am. Chem. Soc.* **138**, 15853–15856 (2016).
49. Liu, Y., Stradins, P. & Wei, S.-H. Van der Waals metal–semiconductor junction: weak Fermi level pinning enables effective tuning of Schottky barrier. *Sci. Adv.* **2**, e1600069 (2016).
50. Radisavljevic, B., Radenovic, A., Brivio, J., Giacometti, V. & Kis, A. Single-layer MoS_2 transistors. *Nat. Nanotech.* **6**, 147–150 (2011).

© 2018 Macmillan Publishers Limited, part of Springer Nature. All rights reserved.

51. Jena, D. & Konar, A. Enhancement of carrier mobility in semiconductor nanostructures by dielectric engineering. *Phys. Rev. Lett.* **98**, 136805 (2007).
52. Rothkirch, L., Link, R., Sauer, W. & Manglus, F. Anisotropy of the electric conductivity of tellurium single crystals. *Phys. Status Solidi (b)* **31**, 147–155 (1969).
53. Si, M., Yang, L., Du, Y. & Ye, P. D. Black phosphorus field-effect transistor with record drain current exceeding 1 A/mm. *2017 75th Ann. Device Res. Conf.* https://dx.doi.org/10.1109/DRC.2017.7999395 (IEEE, 2017).
54. Yang, L. et al. How important is the metal–semiconductor contact for Schottky barrier transistors: a case study on few-layer black phosphorus? *ACS Omega* **2**, 4173–4179 (2017).
55. McClellan, C. J., Yalon, E., Smithe, K. K. H., Suryavanshi, S. V. & Pop, E. Effective n-type doping of monolayer MoS_2 by AlO_x. *2017 75th Ann. Device Res. Conf.* https://dx.doi.org/10.1109/DRC.2017.7999392 (IEEE, 2017).
56. Liu, Y. et al. Pushing the performance limit of sub-100 nm molybdenum disulfide transistors. *Nano Lett.* **16**, 6337–6342 (2016).
57. Kresse, G. & Furthmüller, J. Efficient iterative schemes for ab initio total-energy calculations using a plane-wave basis set. *Phys. Rev. B* **54**, 11169–11186 (1996).
58. Kresse, G. & Joubert, D. From ultrasoft pseudopotentials to the projector augmented-wave method. *Phys. Rev. B* **59**, 1758–1775 (1999).

Acknowledgements

W.Z.W. acknowledges the College of Engineering and School of Industrial Engineering at Purdue University for startup support. W.Z.W. was partially supported by a grant from the Oak Ridge Associated Universities (ORAU) Junior Faculty Enhancement Award Program. Part of the solution synthesis work was supported by the National Science Foundation (grant no. CMMI-1663214). P.D.Y. was supported by the NSF/AFOSR 2DARE Program, ARO and SRC. Q.W. and M.J.K. were supported by the Center for Low Energy Systems Technology (LEAST) and the South West Academy of Nanoelectronics (SWAN). Y.L. acknowledges support from Resnick Prize Postdoctoral Fellowship at Caltech, and startup support from UT Austin. Y.L. and W.A.G. were supported as part of the Computational Materials Sciences Program funded by the US Department of Energy (DOE), Office of Science, Basic Energy Sciences (award no. DE-SC00014607). This work used the computational resources of NREL (sponsored by DOE EERE), XSEDE (NSF ACI-1053575), NERSC (DOE DE-AC02-05CH11231) and the Texas Advanced Computing Center (TACC) at UT Austin. The authors thank F. Fan for discussions.

Author contributions

W.Z.W. and P.D.Y. conceived and supervised the project. W.Z.W., P.D.Y., Y.X.W. and G.Q. designed the experiments. Y.X.W. and R.X.W. synthesized the material. G.Q. and Y.X.W. fabricated the devices. G.Q. and Y.C.D. performed the electrical and optical characterization. S.Y.H. and Y.X.W. performed the Raman measurements under the supervision of X.F.X. and W.Z.W. Q.W. and M.J.K. performed TEM characterization. Y.L. carried out the first-principles calculations under the supervision of W.A.G. Y.X.W. and G.Q. conducted the experiments. W.Z.W., P.D.Y., Y.X.W., G.Q. and R.X.W. analysed the data. W.Z.W. and P.D.Y. wrote the manuscript. Y.X.W., G.Q. and R.X.W. contributed equally to this work. All authors discussed the results and commented on the paper.

Competing interests

The authors declare no competing interests.

Additional information

Supplementary information is available for this paper at https://doi.org/10.1038/s41928-018-0058-4.

Reprints and permissions information is available at www.nature.com/reprints.

Correspondence and requests for materials should be addressed to P.D.Y. or W.W.

Publisher's note: Springer Nature remains neutral with regard to jurisdictional claims in published maps and institutional affiliations.

© 2018 Macmillan Publishers Limited, part of Springer Nature. All rights reserved.